Chinese Chemical Letters 34 (2023) 107125

Contents lists available at ScienceDirect

Chinese Chemical Letters

journal homepage: www.elsevier.com/locate/cclet

Engineering of SnO_2/TiO_2 heterojunction compact interface with efficient charge transfer pathway for photocatalytic hydrogen evolution

Hongli Wang[a], Jianan Liu[a], Xudong Xiao[a,*], Huiyuan Meng[b], Jie Wu[a], Chuanyu Guo[a], Mang Zheng[a], Xiaolei Wang[a,*], Shien Guo[c], Baojiang Jiang[a,*]

[a] Key Laboratory of Functional Inorganic Material Chemistry, Ministry of Education of the People's Republic of China, School of Chemistry and Materials Science, Heilongjiang University, Harbin 150000, China
[b] School of Safety Engineering, Heilongjiang University of Science and Technology, Harbin 150022, China
[c] Institute of Advanced Materials (IAM), College of Chemistry and Chemical Engineering, Jiangxi Normal University, Nanchang 330022, China

ARTICLE INFO

Article history:
Received 12 December 2021
Revised 5 January 2022
Accepted 6 January 2022
Available online 13 January 2022

Keywords:
Photocatalysis
SnO_2-TiO_2 heterojunction
Solvent thermal
Charge transfer
Hydrogen evolution

ABSTRACT

Fabricating an efficient charge transfer pathway at the compact interface between two kinds of semiconductors is an important strategy for designing hydrogen production heterojunction photocatalysts. In this work, we prepared a compact, stable and oxygen vacancy-rich photocatalyst (SnO_2/TiO_2 heterostructure) *via* a simple and reasonable *in-situ* synthesis method. Briefly, $SnCl_2$–$2H_2O$ is hydrolyzed on the TiO_2 precursor. After the pyrolysis process, SnO_2 nanoparticles (5 nm) were dispersed on the surface of ultrathin TiO_2 nanosheets uniformly. Herein, the heterojunction system can offer abundant oxygen vacancies, which can act as active sites for catalytic reactions. Meanwhile, the interfacial contact of SnO_2/TiO_2 grading semiconductor oxide is uniform and tight, which can promote the separation and migration of photogenerated carriers. As shown in the experimental results, the hydrogen production rate of SnO_2/TiO_2 is 16.7 mmol h^{-1} g^{-1} (4.4 times higher than that of TiO_2), which is owing to its good dynamical properties. This work demonstrates an efficient strategy of tight combining SnO_2/TiO_2 with abundant oxygen vacancies to improve catalytic efficiency.

Utilizing renewable solar energy resources to produce hydrogen with abundant water resources is an ideal solution to replace traditional energy and solve dual challenges of global energy and environment [1–3]. At present, the use of semiconductors for photocatalytic decomposition of water to produce hydrogen has attracted extensive attention and research. In recent years, Cu_2O, SnO_2, TiO_2, CdS and other semiconductor materials with excellent photocatalytic hydrogen evolution performance have been developed and utilized by many researchers [4,5]. However, bulk materials severely reduce the accessibility to the active sites and the rate of ion diffusion [6]. These shortcomings will degrade the efficiency of photocatalytic water splitting hydrogen production and hinder the long-term practical application. Replacing traditional bulk structure with ultrathin two-dimensional nanostructure might be an effective solution to address this issue [7–10].

Two-dimensional ultrathin TiO_2 has been widely researched in photocatalytic hydrogen evolution, photocatalytic CO_2 reduction and organic synthesis, due to their unique electronic structure, tunable optical property and ultrathin two-dimensional nanostructure, which are more favorable to reduce the diffusion distance of carriers, provide high surface area and expose rich catalytic activity sites [11–13]. Although the metal oxides composed by single-species ultrathin TiO_2 have achieved great progress, the catalytic performance of single-component photocatalysts is not entirely satisfactory, due to the slow separation and migration kinetics of photogenerated carriers. At present, fabricating tight contact two-component metal-oxide-semiconductors with appropriate bandgap becomes an efficient strategy to promote charge separation and transfer effectively, which can improve the photoreaction activity significantly [14]. Meanwhile, the built-in electric field at the interface of two different defect semiconductor photocatalysts with suitable structures can accelerate the separation and transfer the electron-holes simultaneously [15,16]. Thus, the enhancement of photocatalytic activity depends on the design and fabrication of heterogeneous coupling of different semiconductors with tight in-

* Corresponding authors.
E-mail addresses: xiaoxudong0103@sina.com (X. Xiao), 2018040@hlju.edu.cn (X. Wang), jbj@hlju.edu.cn (B. Jiang).

https://doi.org/10.1016/j.cclet.2022.01.018
1001-8417/

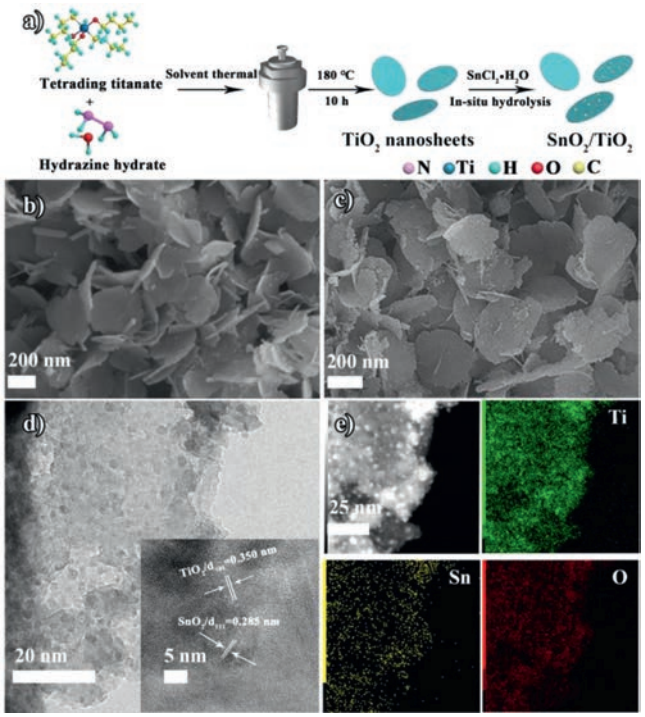

Fig. 1. (a) The synthetic process of SnO_2/TiO_2–1.5. (b, c) SEM images of TiO_2 nanosheets and SnO_2/TiO_2–1.5. (d) TEM and HRTEM images of SnO_2/TiO_2–1.5. (e) TEM image and the corresponding elemental mappings of SnO_2/TiO_2–1.5.

terfacial contact. Considering the excellent electron transfer properties of SnO_2 with the active O-defect sites, combining TiO_2 to form the defect heterostructure can maximize the photogenerated carrier separation efficiency [17,18]. However, the interfacial contact of some heterogeneous structures is not tight enough due to the electrostatic interaction [19]. Therefore, it is urgent to tighten the contact between the interfaces of two kinds of semiconductor photocatalyst, which can benefit in enhancing the reaction kinetics. In particular, the convenient and large-scale preparation of biocomponent oxide photocatalysts with tight contact interfaces to achieve efficient and practical H_2 production remains a great challenge [20,21].

In this work, we first synthesized ultrathin TiO_2 nanosheets by solvothermal method. Then, utilize $SnCl_2{\cdot}2H_2O$ as the Sn source to fabricate SnO_2 on TiO_2 precursor by *in-situ* hydrolysis. Finally, the SnO_2/TiO_2 with high crystallinity can be obtained by high temperature calcination (Fig. 1a). As shown in the experimental results, this synthesis method can avoid damaging the morphology of TiO_2 framework effectively. In addition, the two kinds of metal oxide catalysts can exhibit tighter binding and more abundant oxygen vacancies. Composing SnO_2 with small size on the TiO_2 surface can shorten the band gap, broaden the light response range, and make full use of visible light efficiently. The photocatalytic hydrogen evolution rate can reach 16.7 mmol h^{-1} g^{-1} under the irradiation of AM1.5.

The morphologies of TiO_2 and SnO_2/TiO_2–1.5 are investigated by scanning electron microscopy (SEM), transmission electron microscopy (TEM) and high-resolution transmission electron microscopy (HRTEM) (Figs. 1b-e). As revealed by the SEM images (Fig. 1b and Fig. S1 in Supporting information), the TiO_2 nanosheets synthetized by solvothermal method present uniform thickness and size with the diameter of ~500 nm. Furthermore, the morphology of TiO_2 will change as the variation of hydrazine hydrate adding amount. Increasing the amount of hydrazine hydrate, TiO_2 can gradually grow from conical-rods precursor into a two-dimensional proton titanate nanosheets. Adequate amounts of hydrazine hydrate (4 mL) can promote to form complete nanosheets, which are fries-like assemblies composed by single crystal nanorods. While, adding insufficient hydrazine hydrate (1/2/3 mL) cannot completely formed the structure of nanosheets assembled by nanorods. After the introduction of SnO_2 (Fig. 1c and Fig. S2 in Supporting information), TiO_2 nanosheets still remain intact structure and there are no significant changes on their surface, indicating that the TiO_2 nanosheets synthesized by solvothermal method present good structural stability. Furthermore, the existence of SnO_2 nanoparticles was represented by HRTEM images. It can be obviously observed in the TEM images (Fig. 1d) that the SnO_2 nanoparticles with the diameter of ~5 nm are uniformly distributed on the surface of TiO_2 nanosheets. Meanwhile, two kinds of lattice stripes can be clearly seen in the Fig. 1d with the spacing of 0.350 and 0.285 nm, which are attributed to the 101 faces of TiO_2 and the 111 faces of SnO_2, respectively. The TEM mapping images of SnO_2/TiO_2–1.5 (Ti, O, and Sn) prove that the SnO_2 nanoparticles are distributed on the whole framework of the TiO_2 carrier uniformly. The elemental composition of Ti, O and Sn was also verified by energy spectrum X-ray spectroscopy (EDS, Fig. S3 in Supporting information) and element mapping (Fig. 1e) [22–24]. As shown in Fig. S4 (Supporting information), the specific surface area of TiO_2 and SnO_2/TiO_2–1.5 can be obtained by the nitrogen adsorption-desorption isotherm. Compared with the pure TiO_2, loading SnO_2 can enhance the specific surface area of SnO_2/TiO_2–1.5, providing more active sites for the reaction.

The X-ray diffraction (XRD) and Raman spectra are conducted to further investigate the composition of the synthesized materials. After being calcined at 450 °C (2 °C/min, 2 h) in the air atmosphere, TiO_2 and SnO_2 can recrystallize to form a tight heterojunction. As shown in Fig. 2a, the characteristic peaks can be well matched with the anatase TiO_2 (JCPDS No. 21–1276) and SnO_2 (JCPDS No. 33–1374) standard cards, indicating that the SnO_2/TiO_2–1.5 has been successfully synthesized [25]. It can only observe the anatase TiO_2 and SnO_2 diffraction peaks in the XRD pattens of SnO_2/TiO_2–1.5. Meanwhile, in the Raman spectra (Fig. 2b), it can be observed five typical anatase TiO_2 Raman peaks located at 146.7, 200.1, 402.5, 518.8 and 635.5 cm^{-1}, which are assigned to Eg, Eg, B1g, A1g (B1g), and Eg modes, respectively. There are no other peaks in the Raman spectra of SnO_2/TiO_2–1.5, further indicating that introduce SnO_2 on TiO_2 surface will not change the crystal phase of TiO_2. As compared with pure TiO_2, the peak of SnO_2/TiO_2–1.5 at 600–700 cm^{-1} present a regular blue shift with the increase of the SnO_2 loading amount. And such blue shift of the peak may originate from the replacement of Ti^{4+} by Sn^{4+}, which can change the lattice structure of TiO_2, produce oxygen vacancies, and induce lattice distortion [26,27].

Herein, we utilize the XPS test (Figs. 2c-e and Fig. S5 in Supporting information) to explore the elemental composition and chemical state of SnO_2/TiO_2–1.5. As shown in Fig. 2c, the peaks located at 486.1 eV and 494.5 eV are assigned to Sn $3d_{3/2}$ and Sn $3d_{5/2}$, respectively. And the corresponding peaks of Sn in the SnO_2/TiO_2–1.5 shift to lower binding energy compared with that in the pure SnO_2, meaning that introduce SnO_2 can enhance the electron density of Sn in SnO_2. The peaks of 458.5 eV and 464.2 eV in the Fig. 2d are corresponded to Ti $2p_{3/2}$ and Ti $2p_{1/2}$ of Ti^{4+}, respectively. As compared with pure TiO_2, the peaks of Ti 2p in the SnO_2/TiO_2–1.5 shift ~0.5 eV to higher binding energy, indicating that introduce SnO_2 can decrease the electron density of Ti in TiO_2. As shown in Fig. 2e, the peaks at 529.9 eV and 531.3 eV are attributed to O 1s. The peak at 529.9 eV comes from the lattice oxygen chemically bonded with metal (Sn and Ti), and the binding energy at 531.3 eV comes from the surface oxygen vacancies. Based on the above XPS results, it can be proved the existence of electron transfer between Ti and Sn elements, indicating that the

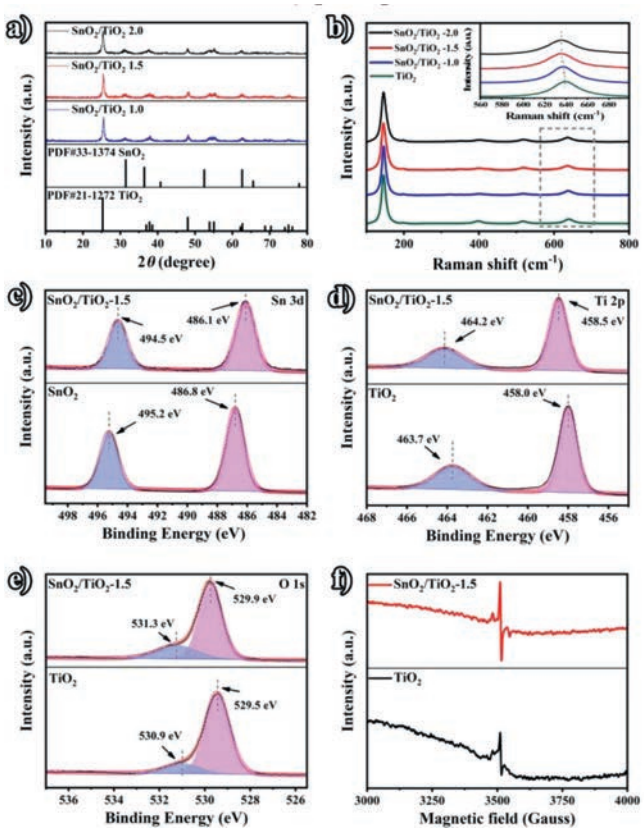

Fig. 2. (a) XRD patterns of SnO_2/TiO_2–1.0, SnO_2/TiO_2–1.5, and SnO_2/TiO_2–2.0. (b) Raman spectra of TiO_2, SnO_2/TiO_2–1.0, SnO_2/TiO_2–1.5 and SnO_2/TiO_2–2.0. High-resolution XPS spectra of (c) Sn 3d, (d) Ti 2p, and (e) O 1s of SnO_2, TiO_2 and SnO_2/TiO_2–1.5. (f) The ESR spectra of TiO_2 and SnO_2/TiO_2–1.5.

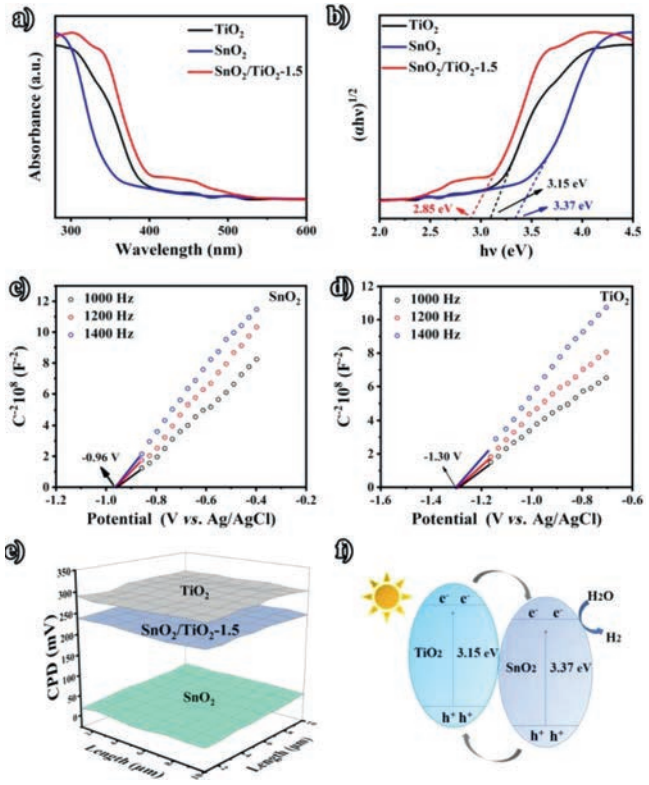

Fig. 3. (a, b) UV-visible diffuse reflectance spectra and determination of the band gaps using Kubelka-Munk function of SnO_2, TiO_2 and SnO_2/TiO_2–1.5. (c, d) Mott-Schottky plots of SnO_2 and TiO_2. (e) Scanning Kelvin probe maps SnO_2, TiO_2 and SnO_2/TiO_2–1.5. (f) Schematic of the photodegradation mechanism of the SnO_2/TiO_2–1.5 porous nanowire nanosheet heterostructures.

close combination of SnO_2/TiO_2–1.5 in favor of charge redistribution. In addition, as revealed by the electron spin resonance (EPR) spectra in Fig. 2f, the oxygen defect in SnO_2/TiO_2 heterostructure is significantly higher than that in the pure TiO_2, which may be due to the occupancy of Sn^{4+} by Ti^{4+} during the high temperature calcination process. This speculation can be supported by the blue shift of Raman spectra in 600–700 cm^{-1} regions after loading SnO_2 on the TiO_2 surface. As the different size of Sn^{4+} and Ti^{4+}, such replacement can form defects, which is favor to decrease the reaction band gap and provide more active sites [28–30].

Fig. 3a presents the UV–visible diffuse reflectance spectra (UV–vis DRS) of SnO_2, TiO_2, and SnO_2/TiO_2–1.5. Compared with the pure SnO_2 and TiO_2, the optical response range of SnO_2/TiO_2–1.5 is expanded. Fig. 3b shows the absorption spectra calculated by Kubelka-Munk function. And the band gap of TiO_2, SnO_2 and SnO_2/TiO_2–1.5 can be calculated by the formula of $(\alpha h\nu)^{1/2} \sim h\nu - E_g$, which are 3.15, 3.37 and 2.85 eV, respectively. The absorption edge presents red-shift with the increasing loading amount of SnO_2, and SnO_2/TiO_2–1.5 exhibits the best light absorption property (Figs. S6 and S7 in Supporting information), indicating that the synergistic effect of SnO_2 and oxygen vacancies can tune the energy band structure of TiO_2 effectively. In order to determine the conduction band (CB) of SnO_2 and TiO_2, the Mott-Schottky measurements were conducted under 1000, 1200, and 1400 Hz (Figs. 3c and d) [31,32]. Both SnO_2 and TiO_2 show positive slopes, which are consistent with the test results of typical n-type semiconductor. According to the calculation of $E_{NHE} = E_{Ag/AgCl} + 0.197$, it can be seen that the energy bands of SnO_2 and TiO_2 locate at −0.763 and −1.103 V *vs.* NHE, respectively. The CB of n-type semiconductor is located around the flat band potential, so it can be determined that the CB edges of SnO_2 and TiO_2 are −0.763 and −1.103 V, respectively. For the further confirmation of the electron transfer between SnO_2 and TiO_2, the work functions (WFs) of SnO_2 and TiO_2 were measured by Kelvin probe. As shown in Fig. 3e, the contact potential difference (CPD) between SnO_2 (TiO_2) and metal probe is 0.023 V (0.29 V). According to the formula of WF = 4.7 + eCPD, it can be calculated that the WFs of SnO_2 and TiO_2 are 4.677 and 4.410 V, respectively. Therefore, the energy level diagram of SnO_2/TiO_2–1.5 can be illustrated by Fig. 3f. Due to the lower work function and the higher Fermi level of TiO_2, combine SnO_2 with TiO_2 can generate the n-n heterojunction. During the illumination process, electrons can transfer from the CB of TiO_2 to the CB of SnO_2. Thus, the electrons are enriched on the surface of SnO_2, which can effectively inhibit the recombination of photogenerated electron-hole pairs and improve the performance of photocatalytic activity [33].

In order to further explore the electron-hole separation efficiency of the composite photocatalyst, the steady-state fluorescence tests of SnO_2 and SnO_2/TiO_2–1.5 have been carried out as shown in Fig. S8a (Supporting information). The intensity of TiO_2 PL peak is significantly higher than that of SnO_2/TiO_2–1.5, owing to the rapid recombination of photogenerated carriers in TiO_2. It is worth noting that loading SnO_2 on the surface of TiO_2 can attenuate the fluorescence intensity, which can prove the inhibition of the rapid recombination for the photogenerated electron-hole pairs and the better capability of capture electrons [34]. The results of wavelength calculation show that the PL peak can match with the band gap of the catalyst calculated by UV–vis DRS. Moreover, it can be concluded that the heterojunction formed by SnO_2 and TiO_2 can improve the charge separation and transmission capacity effectively. Under the irradiation of AM1.5 light source, the photocurrent responses of SnO_2, TiO_2, and SnO_2/TiO_2–1.5 changes periodically with time. When the catalyst is irradiated by light,

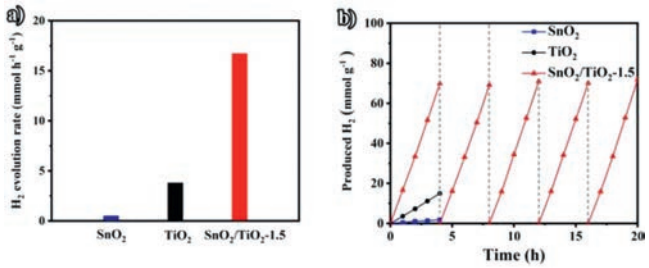

Fig. 4. (a) The H_2 evolution rates for SnO_2, TiO_2, and SnO_2/TiO_2–1.5 (AM 1.5, number of trials: 5 times). (b) Recycling performance of SnO_2, TiO_2 and SnO_2/TiO_2–1.5.

the photoexcited electrons can transfer from the valence band (VB) to the CB, which is the main reason to generate various current changes. It can be found that all samples can preset photocurrent response during the test. The current densities of SnO_2 and TiO_2 are both lower than that of SnO_2/TiO_2–1.5. And the largest photocurrent response of SnO_2/TiO_2–1.5 manifests its prominent carrier generation ability (Fig. S8b in Supporting information), which is consistent with the result of the PL spectra. Moreover, the photocurrent density changed little during the repeated cycling tests, which can prove the good stability of the catalyst [35]. The electrochemical impedance spectra (EIS) of SnO_2, TiO_2 and SnO_2/TiO_2–1.5 are represented in Fig. S9 (Supporting information). As usual in the Nyquist diagram of EIS, the smaller arc radius indicates that the resistance in the charge transfer process is smaller and the carrier separation efficiency is higher. It can be proved that after the introduction of SnO_2 particles, the tightly contact interface of SnO_2/TiO_2–1.5 can provide additional channels for electron transfer and reduce the resistance of electron transfer [36]. Therefore, it is further confirmed that the uniform and compact loading of SnO_2 nanoparticles on TiO_2 nanosheets can accelerate the separation and transmission of photogenerated electron-hole pairs.

Till then, the morphology, composition, and optical characteristic of SnO_2/TiO_2–1.5 heterostructure have been characterized successfully. Based on the advantages of its tight combination, this heterostructure can present efficient charge separation and good charge transfer ability. In addition, the photocatalytic hydrogen production performance of the catalyst has been also evaluated to evaluate its photocatalytic activity. As shown in Fig. 4a, the hydrogen evolution rate of SnO_2, TiO_2, and SnO_2/TiO_2–1.5 are 0.5, 3.8 and 16.7 mmol h^{-1} g^{-1}, respectively. And the hydrogen evolution rate of SnO_2/TiO_2–1.5 is higher than that of SnO_2 and TiO_2 significantly. For SnO_2/TiO_2 composite materials with different SnO_2 loading amounts, SnO_2/TiO_2–1.5 presents the most excellent photocatalytic hydrogen production performance (Fig. S10 in Supporting information). The hydrogen production did not decrease significantly after 5 cycles in the 20-hour photocatalysis process (Fig. 4b), which indicates that SnO_2/TiO_2–1.5 is extremely stable under photocatalytic conditions. In addition, the XRD and SEM images of SnO_2/TiO_2–1.5 are almost unchanged after five cycle testing (Figs. S11 and S12 in Supporting information), indicating that the SnO_2/TiO_2–1.5 we prepared is stable both in structure and morphology during the illumination due to its tight heterogeneous structure [37]. Such excellent photocatalytic performance is originated from the following three reasons: (1) The ultrathin two-dimensional structure of TiO_2 nanosheets, which can improve the accessibility to active sites and ion diffusion rate; (2) The close combination of small SnO_2 on TiO_2 nanosheets, which can promote the rapid separation and transmission of charges; (3) The appropriate oxygen vacancy concentration can adjust the energy band structure of TiO_2 effectively.

In conclusion, we utilized a simple *in-situ* hydrolysis method of $SnCl_2{\cdot}2H_2O$ to load small-size SnO_2 on TiO_2 nanosheets with ultrathin two-dimensional structure. Due to the occupancy of Sn^{4+} by Ti^{4+}, this kind of two-dimensional composite SnO_2/TiO_2–1.5 nanosheets possesses abundant oxygen defects, which can realize the regulation of energy band and provide more active sites in the hydrogen evolution process. In addition, the tight combination of TiO_2 with SnO_2 can promote the charge transfer kinetics and inhibit the recombination of photogenerated electron-hole pairs. The formed material presents excellent performance in solar-driven hydrogen evolution for a long period of time. Overall, this work presents an effective, suitable and simple strategy for tightly combining two semiconductors to efficient charge transfer and may initiate new chances for catalyst development.

Declaration of competing interest

We declare that we have no financial and personal relationships with other people or organizations that can inappropriately influence our work.

Acknowledgments

This work was supported by National Natural Science Foundation of China (No. 21771061) and the Outstanding Youth Fund of Heilongjiang Province (No. JQ 2020B002), the Natural Science Foundation of Heilongjiang Province (No. UNPYSCT-2020006), Natural Science Foundation of Jiangxi Province (No. 20202BABL213002).

Supplementary materials

Supplementary material associated with this article can be found, in the online version, at doi:10.1016/j.cclet.2022.01.018.

References

[1] Q. Wang, T. Hisatomi, Q. Jia, et al., Nat. Mater. 15 (2016) 611–615.
[2] B. Dong, T. Liu, C. Li, F. Zhang, Chin. Chem. Lett. 29 (2018) 671–680.
[3] T. Wei, Y.N. Zhu, X. An, et al., ACS Catal. 9 (2019) 8346–8354.
[4] B. Sun, Y. Chen, L. Tao, et al., ACS Appl. Mater. Interfaces 11 (2019) 2071–2081.
[5] W. Yuan, Z. Xia, L. Li, Chin. Chem. Lett. 24 (2013) 984–986.
[6] G. Cao, N.A. Deskins, N. Yi, Appl. Catal. B 285 (2021) 119748.
[7] X. Bian, S. Zhang, Y. Zhao, R. Shi, T. Zhang, InfoMat 3 (2021) 719–738.
[8] B. Sun, W. Zhou, H. Li, et al., Adv. Mater. 30 (2018) 1804282.
[9] Z. Wang, Q. Wan, Y. Shi, et al., Appl. Catal. B 288 (2021) 120000.
[10] F. Li, X. Xiao, C. Zhao, et al., J. Colloid Interface Sci. 572 (2020) 22–30.
[11] F. Li, Y. Jiao, J. Liu, et al., J. Colloid Interface Sci. 561 (2020) 568–575.
[12] Y. Xiao, S. Guo, G. Tian, et al., Sci. Bull. 66 (2021) 275–283.
[13] J. Liu, Q. Li, X. Xiao, et al., J. Colloid Interface Sci. 590 (2021) 1–11.
[14] S. Hu, P. Qiao, L. Zhang, et al., Appl. Catal. B 239 (2018) 317–323.
[15] Y. Zhao, Y. Zhao, R. Shi, et al., Adv. Mater. 31 (2019) 1806482.
[16] W. Zhang, H. He, Y. Tian, et al., Chem. Sci. 10 (2019) 1664–1670.
[17] X. Deng, Y. Chen, J. Wen, et al., Sci Bull. 65 (2020) 105–112.
[18] L. Zhang, X. He, X. Xu, et al., Appl. Catal. B 203 (2017) 1–8.
[19] Y. Zhang, L. Ran, Z. Li, et al., Trans. Tianjin Univ. 27 (2021) 348–357.
[20] T. Lin, Z. Pi, M.C. Gong, et al., Chin. Chem. Lett. 18 (2007) 241–243.
[21] Y. Xiao, S. Guo, G. Tian, et al., Sci. Bull. 66 (2021) 275–283.
[22] S. Sun, H. Ding, L. Mei, et al., Chin. Chem. Lett. 31 (2020) 2287–2294.
[23] Y. Jiang, Y. Qin, T. Yu, S. Lin, Chin. Chem. Lett. 32 (2021) 1823–1826.
[24] X. Li, J. Wang, Z. Hu, M. Li, K. Ogino, Chin. Chem. Lett. 29 (2018) 166–170.
[25] X. Guo, J. Wan, X. Yu, Y. Lin, Chemosphere 164 (2016) 421–429.
[26] W. Guo, Y. Qin, C. Liu, et al., Appl. Catal. B 298 (2021) 120526.
[27] C. Cheng, L. Wen, Mater. Res. Bull. 129 (2020) 110912.
[28] S. Ren, W. Liu, J. Mater. Chem. A 4 (2016) 2236–2245.
[29] X. Li, X. Zhang, R. Wang, et al., J. Power Sources 336 (2016) 298–306.
[30] Q. Wan, Y. Chen, S. Zhou, J. Lin, S. Lin, J. Mater. Chem. A 9 (2021) 14064–14073.
[31] D. Spanu, S. Recchia, S. Mohajernia, P. Schmuki, M. Altomare, Appl. Catal. B 237 (2018) 198–205.
[32] M. Chen, J. Yang, Y. Liu, et al., J. Mater. Chem. A 3 (2015) 1405–1409.
[33] D. Zhao, Y. Wang, C. Dong, et al., Nat. Energy 6 (2021) 388–397.
[34] A. Farhadi, M.R. Mohammadi, M. Ghorbani, J. Photochem. Photobiol. A: Chem. 338 (2017) 171–177.
[35] S. Zhang, L. Zhao, B. Huang, X. Li, Sens. Actuator. B: Chem. 319 (2020) 128264.
[36] L. Guo, H. Yin, M. Xu, et al., ACS Sens. 4 (2019) 2724–2729.
[37] X. Xu, G. Yang, J. Liang, et al., J. Mater. Chem. A 2 (2014) 116–122.